J. Phys. Chem. A **2008,** *112,* 10469–10480

Energetics and Mechanisms of C−H Bond Activation by a Doubly Charged Metal Ion: Guided Ion Beam and Theoretical Studies of $Ta^{2+} + CH_4$

Laura G. Parke, Chris S. Hinton, and P. B. Armentrout*

Department of Chemistry, University of Utah, Salt Lake City, Utah 84112

Received: June 13, 2008; Revised Manuscript Received: July 29, 2008

A guided ion beam tandem mass spectrometer is used to study the kinetic-energy dependence of doubly charged atomic tantalum cations (Ta^{2+}) reacting with CH_4 and CD_4. As for the analogous singly charged system, the dehydrogenation reaction to form $TaCH_2^{2+} + H_2$ is exothermic. The charge-transfer reaction to form $Ta^+ + CH_4^+$ and the charge-separation reaction to form $TaH^+ + CH_3^+$ are also observed at low energies in exothermic processes, as is a secondary reaction of $TaCH_2^{2+}$ to form $TaCH_3^+ + CH_3^+$. At higher energies, other doubly charged products, TaC^{2+} and $TaCH_3^{2+}$, are observed, although no formation of TaH^{2+} was observed. Modeling of the endothermic cross sections provides 0 K bond dissociation energies (in electronvolts) of $D_0(Ta^{2+}-C) = 5.42 \pm 0.19$ and $D_0(Ta^{2+}-CH_3) = 3.40 \pm 0.16$. These experimental bond energies are in poor agreement with density functional calculations at the B3LYP/HW+/6−311++G(3df,3p) level of theory. However, the $Ta^{2+}-C$ bond energy is in good agreement with calculations at the QCISD(T) level of theory, and the $Ta^{2+}-CH_3$ bond energy is in good agreement with density functional calculations at the BHLYP level of theory. Theoretical calculations reveal the geometric and electronic structures of all product ions and are used to map the potential energy surface, which describes the mechanism of the reaction and key intermediates. Both experimental and theoretical results suggest that TaH^+, $TaCH_2^{2+}$, and $TaCH_3^{2+}$ are formed through a $H-Ta^{2+}-CH_3$ intermediate.

1. Introduction

Relatively few studies of the reactivity of doubly charged atomic transition metal cations have been performed, although the mass spectrometric study of multiply charged complexes has become very active during the last two decades.[1−4] The dearth of atomic metal dication reactivity studies is partly a consequence of the difficulty in generating doubly charged atomic ions relative to singly charged ions. Further, it was generally believed that multiply ionized ions would undergo charge transfer reactions exclusively. Tonkyn and Weisshaar[5] were the first to report that the early transition metal Ti^{2+} undergoes a clustering reaction with methane at thermal energies, hydride transfer with ethane, and a simple charge transfer reaction with propane. This observation encouraged Freiser and co-workers to look at the behavior of other doubly charged early transition metals, using Fourier transform ion cyclotron resonance (FTICR) mass spectrometry. For Nb^{2+}, Freiser and co-workers found dehydrogenation to be the predominant pathways in the reaction with methane and ethane, whereas propane and butane reacted by charge transfer.[6,7] For Zr^{2+}, dehydrogenation of methane was again found to be the predominant pathway, with a small percentage (4%) of the hydride abstraction product, ZrH^+, and no charge transfer products, $Zr^+ + CH_4^+$.[8] Zr^{2+} undergoes dehydrogenation and demethanation reactions and hydride abstraction with ethane and propane. Propane also exhibits methide abstraction as well as charge transfer, which becomes the predominant reaction pathway with butane. For Ta^{2+} reacting with methane, dehydrogenation is the major pathway, but formation of the hydride abstraction product, $TaH^+ + CH_3^+$, along with charge transfer, $Ta^+ + CH_4^+$ is also observed.[8] Freiser and co-workers report that reactions of Ta^{2+} with longer chain alkanes result in exclusive charge transfer. In contrast, La^{2+} is unreactive with methane and ethane, but propane and butane yield dehydrogenation and alkane loss, as well as charge-separation reaction products in the case of butane.[9]

In the present study, we reexamine the reaction of Ta^{2+} with methane and its isotopologue, CD_4. Ta^{2+} is produced exclusively in its ground state, a^4F ($5d^3$), using a dc discharge/flow tube ion source. In contrast to previous work that was limited to thermal reactions, our study is the first to examine the kinetic energy dependence of reactions of atomic multiply charged metal cations. Thus, this study provides quantitative thermochemical and mechanistic information that complements previous studies and allows an assessment of theoretical approaches for evaluating these highly charged heavy metal species. For this reason, a complete theoretical investigation of all product ions and the transition states and intermediates along the potential energy surfaces accessible are also pursued.

2. Experimental and Theoretical Methods

2.1. General Procedures. These experiments were performed using a guided ion beam tandem mass spectrometer described in detail elsewhere.[10] Ions are formed in a direct current discharge/flow tube (DC/FT) source described below, extracted from the source, then accelerated and passed through a magnetic sector momentum analyzer for mass analysis. Reactant ions containing the ^{181}Ta isotope (99.99% natural abundance) are selected, decelerated to a desired kinetic energy, and focused into an octopole guide that radially traps the ions using radio frequency electric fields.[11,12] While in the octopole, the ions pass through a static gas cell that contains the neutral reaction partner at a pressure of less than ~0.3 mTorr, to ensure that multiple ion−molecule collisions do not occur. This was verified by examining the pressure dependence of the reaction

---

* Corresponding author.

10.1021/jp8052295 CCC: $40.75

cross sections. The remaining reactant and product ions are confined in the radial direction in the guide until they drift out of the gas cell and are focused into a quadrupole mass filter for mass analysis. The ions are then detected by a secondary electron scintillation ion detector, using standard pulse counting techniques. After correcting for background signals, ion intensities are converted to absolute cross sections, as described previously.[13] The uncertainties in absolute cross sections are estimated at ±20%. The quadrupole is operated in a mode designed to optimize ion transmission to ensure accurate cross section magnitudes, such that product cross sections having adjacent masses have been corrected for mass overlap. Because the various product ions have distinct energy dependences, such corrections are unambiguous in the present case as verified by equivalent cross section determinations using both CH_4 and CD_4 reactants (see below).

The kinetic energy is varied in the laboratory frame by scanning the DC bias on the octopole rods with regard to the potential of the ion source region. The nominal potential difference between these regions ($V_{Laboratory}$) is converted to the center-of-mass (CM) frame relative ion energy using the formula $E_{CM} = 2 \times V_{Laboratory}\, m/(m + M)$, where m and M are the neutral and ionic reactant masses, respectively. The kinetic energy distribution of the reactant ion and the thermal motion of the neutral reactant gas (Doppler broadening) both contribute to broaden the cross sections.[14,15] The octopole beam guide is used as a retarding potential analyzer, as described previously,[13] to determine both the absolute zero of the energy scale and the full width at half-maximum of the kinetic energy distribution of the ions. This distribution is nearly Gaussian and independent of energy. The full width at half-maximum is 0.2 − 0.6 eV (potential in the laboratory frame) in these studies (0.03−0.12 eV in the CM frame). Uncertainties in the absolute energy scale are ±0.01 eV (CM).

2.2. Ion Source. Atomic Ta^{2+} cations are formed in the DC/FT source, which utilizes a tantalum cathode held at high negative voltage (0.7−1.5 kV). A flow of approximately 90% He and 10% Ar passes over the cathode at a total pressure of 0.3−0.4 Torr and ambient temperature. Ar^+ ions created in the resultant discharge are accelerated toward the cathode, thereby creating Ta^+ and Ta^{2+} ions. The ions then undergo $\sim 10^5$ collisions with He and $\sim 10^4$ collisions with Ar in the meter-long flow tube before entering into the guided ion beam apparatus. These source conditions are identical to those used previously to generate numerous singly charged transition metal cations, and it is anticipated that collisional cooling of the electronic states by the bath bases will be similar for both charge states. Previous work shows that, when compared to a surface ionization source, the DC/FT source generates Sc^+,[16] Fe^+,[17] Co^+,[18] Ni^+,[19] Ru^+,[20] Rh^+,[20] and Pd^+,[20] ions with an average electronic temperature of 700 ± 400 K, and Y^+, Zr^+, Nb^+, and Mo^+ ions with an average electronic temperature of 300 ± 100 K.[21] Even at an elevated electronic temperature (1100 K), a pure beam of ^4F ground-state Ta^{2+} ions is produced, having a calculated distribution of 94.26% $^4F_{3/2}$ ($5d^3$, 0.000 eV), 5.29% $^4F_{5/2}$ ($5d^3$, 0.312 eV), 0.33% $^4F_{7/2}$ ($5d^3$, 0.602 eV), 0.07% $^4F_{3/2}$ ($6s5d^2$, 0.687 eV), and 0.03% $^4F_{9/2}$ ($5d^3$, 0.840 eV), with all other spin−orbit levels (with energies 0.891 eV and higher) having populations less than 0.01%. (All energies taken from ref 22). At 700 K, the populations are 99.14%, 0.85%, 0.01%, and <0.001%, respectively; and at 300 K, Ta^{2+} ions are produced exclusively in their $^4F_{3/2}$ ground state (<0.001% in higher spin orbit states). Conservatively, the average electronic energy of the reactant Ta^{2+} ions is estimated to be 0.003 +0.019/−0.003 eV.

2.3. Data Analysis. To determine E_0, the energy threshold for product formation, the kinetic energy dependence of product cross sections is analyzed. The apparent threshold observed under laboratory conditions lies below E_0 because of the Maxwell−Boltzmann velocity distribution, the internal energy of the neutral reactants, and the kinetic energy distribution of the reactant ions. Previous theoretical and experimental work has shown that endothermic cross sections can be modeled using eq 1[23−25]

$$\sigma(E) = \sigma_0 \sum g_i (E + E_i + E_{el} - E_0)^n / E \qquad (1)$$

where σ_0 is an energy-independent scaling parameter, E is the relative kinetic energy of the reactants, E_i is the internal energy of the reactants, E_{el} is the average electronic energy of the reactant ion, E_0 is the reaction threshold at 0 K, and n is an adjustable parameter that determines the shape of the cross section. The summation is over all possible rovibrational states of the neutral reactant with energies E_i and relative populations g_i, where $\Sigma g_i = 1$. The various sets of vibrational frequencies and rotational constants used to determine E_i in this study are taken from the literature for CH_4 and CD_4.[26] Equation 1 is convoluted over both the neutral and the ion kinetic energy distributions prior to comparison with the data. All adjustable parameters, E_0, σ_0, and n, are then optimized to give the best reproduction of the data using a nonlinear least-squares analysis.[24,25] The average values obtained for each parameter over a range of best fits to several independent data sets are the values reported for E_0, σ_0, and n. The resultant uncertainties are one standard deviation. The uncertainties reported for E_0 also contain the uncertainty in the absolute energy scale (±0.05 eV, laboratory) and electronic energy, ±0.02 eV.

2.4. Theoretical Calculations. In the present study, most quantum chemistry calculations are computed with the B3LYP hybrid density functional method[27,28] and performed with the Gaussian 03 suite of programs.[29] This level of theory was used because it provides reasonable results for analogous reactions of methane with other heavy transition metal atomic ions: Pt^+,[30] Re^+,[31] W^+,[32] Ir^+,[33] Hf^+,[34] Au^+,[35] and Ta^+.[36] All thermochemistry reported here is corrected for zero-point energy effects. Because many of the transition states of interest have bridging hydrogens, the relatively large 6−311++G(3df,3p) basis set is used for carbon and hydrogen. This basis set provides bond energies for the hydrocarbon species that are comparable (within 0.08 eV) to experimental results: $H-CH_3$ (4.406 vs 4.480 eV), H_2-CH_2 (4.666 vs 4.713 eV), H−CH (4.332 vs 4.360 eV), C−H (3.532 vs 3.465 eV), and H−H (4.505 vs 4.478 eV). (See Table 1 of ref 30 for thermochemistry used for all H, D, CH_x, and CD_x species.) The Los Alamos double-ζ basis set (LANL2DZ) describes the outer valence electrons and the relativistic effective core potential (ECP) of Hay−Wadt (HW)[37] describes the 60 core electrons of tantalum. Because this basis set is optimized for neutral atoms, whereas the charge on Ta^{2+} differentially contracts the 6s orbitals compared to the 5d orbitals, an altered valence basis set as described by Ohanessian et al.,[38] denoted by HW+, is used throughout our calculations for Ta^{2+}.

The most relevant choice for a level of theory for the first- and third-row transition metal methyl cations has been studied by Holthausen et al.[39] and for first-row transition metal methylene cations by Holthausen, Mohr, and Koch.[40] For the metal methyl complexes (constrained to C_{3v} symmetry), these authors used B3LYP and Becke-half-and-half-LYP (BHLYP) functionals and the QCISD(T) method with a basis set consisting of a polarized double-ζ basis on C and H and the Hay−Wadt relativistic ECP with valence electrons added. These authors concluded that, for the first-row MCH_3^+ species (M = Sc−Cu), where experimental results are available for all metals,[41,42] the B3LYP functional overbinds, with a mean absolute deviation (MAD) from experiment of 0.41 eV. In contrast, better comparison to experimental work was obtained with the BHLYP functional and the QCISD(T) method, with MADs of 0.18 and 0.20 eV, respectively. For the metal methylene cation complexes,[40] the B3LYP functional predicts bond energies in good agreement with experimental data, whereas the performance of the BHLYP functional predicts bond energies consistently below experimental data. On the basis of these results, the present study includes calculations for the various product ions using the BHLYP functional and the Stuttgart−Dresden (SD) ECP[43] for Ta^{2+}, as well as QCISD(T) calculations using the HW+ ECP. Unless otherwise noted, our theoretical results will refer to the B3LYP/HW+/6−311++G(3df,3p) level of theory.

We calculated a $^4F(5d^3)$ ground state for Ta^{2+}, a $^2P(5d^3)$ excited state at 0.680 eV, and a $^4F(6s^15d^2)$ excited state at 0.895 eV, using the HW+ basis set and B3LYP level of theory. For the B3LYP/SD, BHLYP/HW+, and BHLYP/SD combinations of functional/basis set, we found excitation to the doublet state to be 0.666, 0.728, and 0.717 eV, respectively, and excitation to the quartet state to be 0.758, 0.985, and 0.911 eV, respectively, demonstrating that the atomic excitations are largely independent of the theoretical method chosen. For the QCISD(T)/HW+ level of theory, we found much lower excitation energies of 0.106 and 0.472 eV, respectively. No appreciable spin contamination was found for the different levels of theory for any of these states. The quartet-doublet excitation energies can be compared to experimental values (average of the spin−orbit levels for each state) of 0.381 eV for a $^2P(5d^3)$ excited state and 0.990 for a $^2D(5d^3)$ excited state,[22] such that the density functional theoretical values fall between these two values. The experimental excitation energy for the $^4F(6s^15d^2)$ state is 0.732 eV, in reasonable agreement with the theoretical values. The theoretically calculated IE of Ta^+ is relatively insensitive to the level of theory used: 15.2, 15.2, 14.9, 14.8, and 14.6 eV using B3LYP/HW+, B3LYP/SD, BHLYP/HW+, BHLYP/SD, and QCISD(T)/HW+. In all cases, these values are low compared with the experimental value of 16.2 ± 0.5 eV.[44]

3. Experimental Results

3.1. Reaction of Ta^{2+} with Methane. Reaction of CH_4 with Ta^{2+} yields the primary products indicated in reactions 2−6.

$$Ta^{2+} + CH_4 \rightarrow Ta^+ + CH_4^+ \qquad (2)$$

$$\rightarrow TaH^+ + CH_3^+ \qquad (3)$$

$$\rightarrow TaCH_3^{2+} + H \qquad (4)$$

$$\rightarrow TaCH_2^{2+} + H_2 \qquad (5)$$

$$\rightarrow TaC^{2+} + 2H_2 \qquad (6)$$

In addition, several higher order products are observed as the pressure of methane is increased. These products, which are easily identified because their cross sections depend on the methane pressure, include reactions 7−10.

$$CH_3^+ + CH_4 \rightarrow C_2H_5^+ + H_2 \qquad (7)$$

$$TaCH_2^{2+} + CH_4 \rightarrow TaCH_3^+ + CH_3^+ \qquad (8)$$

$$\rightarrow TaC_2H_2^{2+} + 2H_2 \qquad (9)$$

$$TaC_2H_2^{2+} + CH_4 \rightarrow TaC_3H_4^{2+} + H_2 \qquad (10)$$

Reaction 8 is discussed further below and reactions 9 and 10 are explored more thoroughly in the next section. We anticipated that we should also observe the secondary reaction 11,

$$CH4_4^+ + CH_4 \rightarrow CH_5^+ + CH_3 \qquad (11)$$

Because the intensity of the primary CH_4^+ product is already small, the secondary CH_5^+ product was not observed because it would be at least an order of magnitude smaller even at the highest methane pressures used. Reactions 7 and 11 deplete the primary CH_3^+ and CH_4^+ products at the lowest energies where the residence time of these products in the reaction chamber is the longest. This tends to scatter these products even further, such that collection of these secondary product ions is inefficient.

Figure 1 shows analogous results for Ta^{2+} reacting with CD_4, which provides cross sections consistent with those obtained for reaction with CH_4. This agreement verifies that the cross sections are accurately ascertained even though the mass-to-charge separation between some products is only 0.5 *m/z* in the

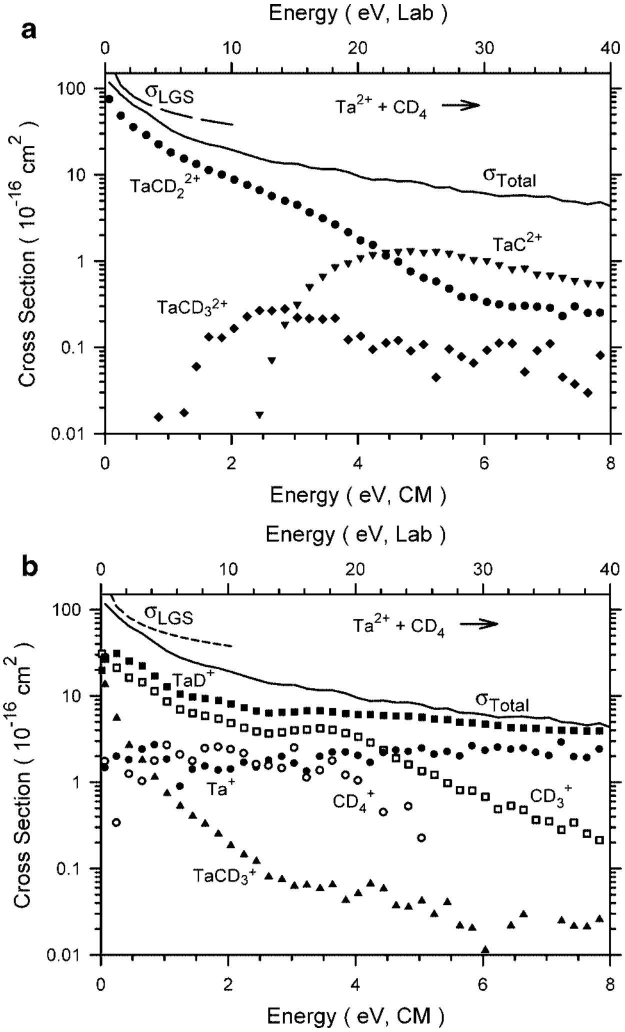

Figure 1. Cross sections for reaction of Ta^{2+} (^4F) with CD_4 as a function of kinetic energy in the center-of-mass frame (lower axis) and laboratory frame (upper axis). Part a shows products retaining the 2+ charge, whereas part b shows products formed by charge transfer and charge separation. The $TaCD_3^+$ cross section has a distinct pressure dependence, and the results shown here correspond to $P(CD_4)$ = 0.4 mTorr.

TABLE 1: Rates (10^{-10} cm^3 s^{-1}) and Reaction Efficiencies (%, in Parentheses) for Reaction of Ta^{2+} with Methane

product	this work		previous work[a]
	CH_4	CD_4	CH_4
Ta^+	0.12 ± 0.04 (0.6 ± 0.2)	0.17 ± 0.03 (1.0 ± 0.2)	4.9 ± 2.5 (25 ± 13)
TaH^+	3.5 ± 0.7 (18 ± 4)	4.2 ± 1.0 (24 ± 6)	4.5 ± 2.3 (23 ± 12)
CH_3^+	4.9 ± 1.8 (25 ± 9)	3.7 ± 0.7 (21 ± 4)	
$TaCH_2^{2+}$	9.2 ± 2.8 (47 ± 14)	8.0 ± 1.6 (45 ± 9)	10.0 ± 5.0 (52 ± 27)
Total	13.5 ± 3.4 (69 ± 17)	12.1 ± 2.4 (69 ± 14)	19.4 ± 9.7 (100 ± 50)
LGS[b]	19.5	17.6	19.5

[a] Reference 8. [b] Langevin−Gioumousis−Stevenson collision rate constant, ref 46.

CH_4 system (but at least 1.0 *m*/*z* in the CD_4 system). Only results for the perdeuterated species are shown here because use of CD_4 reduces mass overlap, allowing for a more accurate measurement of product intensities over a greater energy range (in particular of $TaCH_3^{2+}$, which is much smaller than $TaCH_2^{2+}$, only 0.5 *m*/*z* away). In the following discussion, the results will be generally described using perprotio species for both CH_4 and CD_4 systems.

As can be seen in Figure 1, formation of $Ta^+ + CH_4^+$ (reaction 2), $TaH^+ + CH_3^+$ (reaction 3), and $TaCH_2^{2+} + H_2$ (reaction 5) exhibit no kinetic energy barriers to the overall reaction and hence must be exothermic. For the charge transfer reaction 2, this is consistent with fact that the ionization energy of CH_4, 12.61 ± 0.01 eV,[45] is less than the second ionization energy of Ta, 16.2 ± 0.5 eV.[44] For reaction 3, this observation is consistent with known thermochemical data: $D_0(CH_3{-}H) = 4.480 \pm 0.006$ eV,[45] $IE(CH_3) = 9.84 \pm 0.01$ eV,[45] and $D_0(Ta^+{-}H) = 2.39 \pm 0.08$,[36] which indicate that this reaction is exothermic by 4.26 ± 0.51 eV. As required by reactions 2 and 3, the magnitudes of the CH_4^+ and Ta^+ cross sections and those of CH_3^+ and TaH^+ are similar below about 3 and 4 eV, respectively (Figure 1b). This confirms that the collection of these products is quite good in our instrument, even with the high relative translational energy that presumably results from the Coulomb repulsion between these products (see below). At high energies (above about 4 eV for both reactions), the CH_4^+ and CH_3^+ cross sections decline, whereas the Ta^+ and TaH^+ cross sections stay relatively constant. This is attributable to the efficiency with which the product ions are transmitted through the quadrupole mass filter, although contributions from the transmission between the octopole and the quadrupole may also contribute. Because the Ta^+ and TaH^+ products retain the heavy tantalum nucleus, they retain most of the momentum in the laboratory frame associated with the reactant Ta^{2+} ion, and therefore are transmitted through the quadrupole filter efficiently at all collision energies. The lighter mass CH_4^+ and CH_3^+ products need not acquire much momentum in the laboratory frame, and therefore their transmission through the quadrupole is eventually limited once the DC bias on the octopole reaction region exceeds the DC bias voltage on the quadrupole mass filter, as verified by a rough correlation between the onset of the declines in the cross section in the laboratory frame with the DC bias voltage applied to the quadrupole. Exactly where this deviation occurs is dependent on the details of the dynamics of the reaction and is a rough measure of how forward scattered these products are in the laboratory frame.

The most probable reaction is formation of $TaCH_2^{2+}$ in the dehydrogenation reaction 5. This product ion has a cross section that declines as $E^{-0.5\pm0.1}$ below 1.5 eV, the same energy dependence as the Langevin−Gioumousis−Stevenson (LGS) collision cross section.[46] Likewise, the cross sections for formation of TaH^+ and CH_3^+ in reaction 3 decline as $E^{-0.4\pm0.1}$ below 1.5 eV. In contrast, cross sections for the charge transfer reaction 2, formation of Ta^+ and CH_4^+, vary little with kinetic energy throughout the entire range examined. As noted above, the cross section for formation of $TaCH_3^+$ shows a dependence on the reactant methane pressure, which is consistent with its energy dependence as it declines as $E^{-1.0\pm0.1}$ below 1.5 eV. Such an energy dependence is consistent with sequential exothermic reactions that each follow the $E^{-0.5}$ LGS energy dependence.

3.2. Rate Constants. To compare our results to the literature, we convert our cross sections to rate constants using eq 12,[13]

$$k(\langle E\rangle) = \nu\sigma(E) \tag{12}$$

where $\nu = (2E/\mu)^{1/2}$ and $\mu = mM/(m + M)$, the reduced mass of the reactants. This rate constant depends on the mean energy of the reactants, which includes the average thermal motion of the neutral, eq 13,

$$\langle E\rangle = E + (3/2)\gamma k_B T \tag{13}$$

where $\gamma = M/(m + M)$. Using this equation, we obtain the rates shown in Table 1 for reactions with CH_4 and CD_4. Table 1 also lists the experimental reaction efficiencies compared with the LGS rates of 19.5×10^{-10} cm^3/s (CH_4) and 17.6×10^{-10} cm^3/s (CD_4), using a polarizability volume for methane of 2.56 Å^3.[47] For the dominant reaction 5, the reaction efficiencies for the two systems agree nicely, and further, our result for CH_4 agrees well with results obtained by FT ICR mass spectrometry.[8] Likewise, for reaction 3, the rates for both ionic products (TaH^+ and CH_3^+) agree within experimental uncertainty, and the efficiencies agree for both the CH_4 and the CD_4 systems. Again our values agree within experimental uncertainties with the rate constant obtained by FT ICR mass spectrometry, where only the TaH^+ product was monitored.[8] For the charge transfer reaction 2, our rate constants for formation of CH_4^+ and CD_4^+ are not included in Table 1 because of poor collection efficiency at thermal energies for these two products. In comparison with the LGS collision rate, we find that reaction 2 occurs with efficiencies near 1%, which disagrees severely with the results obtained by FT ICR mass spectrometry, 25 ± 13% efficiency, where only the Ta^+ product was monitored.[8] However, Freiser and co-workers comment that the amount of Ta^+ formed as a result of simple charge transfer observed in the FT ICR could be overestimated because of difficulties associated with multiple reactions between product ions and methane or between Ta^{2+} and residual gases in the FT ICR cell.[8] Furthermore, it is possible that the Ta^{2+} ions, which were generated with a Nd:YAG pulsed laser in the ICR experiments, could have had a population of excited electronic states that might undergo charge transfer more readily.

When the thermal rate constants for reactions 2, 3, and 5 are combined (taking the average rate for TaH^+ and CH_3^+), the total reaction rates are $(13.5 \pm 3.4) \times 10^{-10}$ cm^3/s for CH_4 and $(12.1 \pm 2.4) \times 10^{-10}$ cm^3/s for CD_4, such that the overall reaction efficiencies are 69 ± 17% and 69 ± 14%, respectively.

For the FT ICR results, the overall reaction efficiencies were quoted as 100 ± 50% for the CH_4 system, within the combined experimental errors. The agreement is improved once the overestimation of the charge transfer reaction,[8] noted above, is accounted for.

As noted above, formation of $TaCH_3^+$ is observed as a secondary reaction and attributed to reaction 8. This reaction was not observed in the FT ICR study.[8] Reaction 8 is calculated to be exothermic by less than 4.6 ± 0.5 eV, given thermochemical data above, $D_0(Ta^+{-}CH_3) = 2.69 \pm 0.14$ eV[36] and $D_0(Ta^{2+}{-}CH_2) > 4.7$ eV, which comes from the observation that reaction 5 is exothermic. Interestingly, formation of the $TaCH_3^+$ product can conceivably occur in the primary reaction 14,

$$Ta^{2+} + CH_4 \rightarrow TaCH_3^+ + H^+ \tag{14}$$

which is exothermic by 0.81 ± 0.52 eV, given thermochemistry from above and IE(H) = 13.59844 eV.[45] Nevertheless, this primary reaction does not appear to occur for reasons discussed further below. It might be thought that whether reaction 14 occurs or not could be verified by detecting the H^+ product; however, because of its low mass, trapping of this species in the octopole is inefficient at the rf frequency used (about 7 MHz).

Finally, we note that neither we nor Freiser and co-workers observed a $TaCH_2^+$ product, which could be formed in reaction 15.

$$Ta^{2+} + CH_4 \rightarrow TaCH_2^+ + H_2^+ \tag{15}$$

Given $D_0(Ta^+{-}CH_2) = 4.81 \pm 0.03$ eV,[36] this reaction is calculated to be exothermic by 0.87 ± 0.52 eV. Ultimately, the failure to observe this process can be related to the relatively large ionization energy of H_2, IE = 15.43 eV,[45] as discussed further below.

3.3. Multiple Collision Dehydrogenation Reactions.

As previously observed by Freiser and co-workers,[8] the primary $TaCH_2^{2+}$ products formed in reaction 5 react further with methane (reactions 9 and 10). Indeed, the FT ICR study observed sequential dehydrogenation reactions with up to six methane molecules. In addition to the double dehydrogenation reaction 9, the single dehydrogenation reaction 16 was also observed in the FTICR study but with a branching ratio of only 10% compared with 90% for reaction 9.

$$TaCH_2^{2+} + CH_4 \rightarrow TaC_2H_4^{2+} + H_2 \tag{16}$$

Under our experimental conditions, we observe that Ta^{2+} successively dehydrogenates three methane molecules to form a sequence of $TaC_xH_y^{2+}$, $x = 1-3$, product ions. (Reaction 16 was not observed, consistent with the low probability seen in the FTICR study.) The cross sections for these product ions (Figure 2) display a distinct dependence on methane pressure over the range examined, 0.1 to 0.4 mTorr. It can be seen that the cross section for the primary $TaCH_2^{2+}$ product ion decreases as the methane pressure increases, verifying that it reacts away in subsequent collisions. In contrast, the cross sections for the $TaC_2H_2^{2+}$ and $TaC_3H_4^{2+}$ product ions increase with increasing methane pressure, showing that they result from higher order reactions. At the lowest energies, it is found that the $TaC_2H_2^{2+}$ cross section doubles in magnitude for a two-fold increase in methane pressure, demonstrating that it is formed in a second order reaction, whereas the $TaC_3H_4^{2+}$ cross section increases by a larger factor for the same pressure increase, showing that it is a third order reaction. The energy dependences of both of these product ions indicate that each of these subsequent reactions are exothermic, having no barriers in excess of the energy of the reactants.

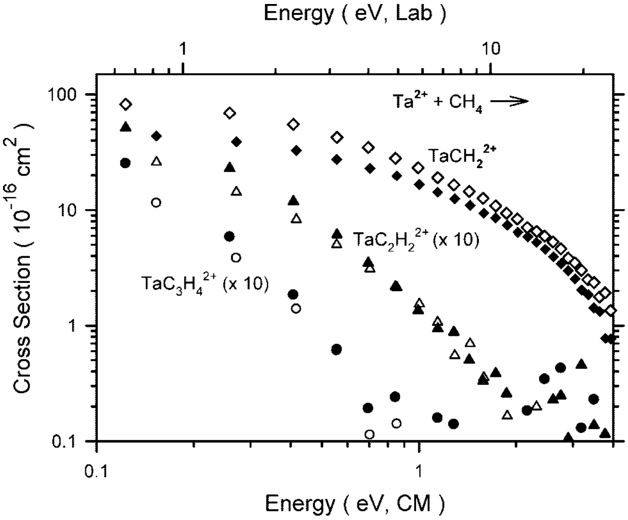

Figure 2. Cross sections for multiple reactions of Ta^{2+} (^4F) with CH_4 as a function of kinetic energy in the center-of-mass frame (lower axis) and laboratory frame (upper axis). Open and closed symbols show results taken at methane pressures of 0.20 and 0.41 mTorr, respectively.

4. Thermochemical and Theoretical Results

The endothermic cross sections for TaC^{2+} and $TaCH_3^{2+}$ are analyzed using eq 1 and the optimum values of the fitting parameters are listed in Table 2. Because the rotational, translational, and vibrational energy distributions are included in the modeling, all E_0 thresholds determined by eq 1 correspond to 0 K values. The BDEs of these species are calculated from the measured thresholds using eq 17,

$$D_0(Ta^{2+}{-}L) = D_0(R{-}L) - E_0 \tag{17}$$

where the $D_0(R{-}L)$ values can be calculated using the heats of formation summarized previously.[30] This expression assumes that there are no activation barriers in excess of the endothermicity, which is generally the case for ion−molecule reactions because of the long-range attractive forces that are present.[25] A summary of the BDEs derived and a comparison to theoretical values are given in Table 3. A summary of the B3LYP theoretical results for the energies and structures of the product ions and their excited states is given in Supporting Information, Tables S1 and S2. The following sections discuss the results in detail for each of the species.

4.1. $Ta^{2+}{-}H$.

The doubly charged TaH^{2+} species was not observed, however, for completeness, calculations were performed for this species and included here. For $Ta^{2+}{-}H$, we calculate a bond dissociation energy of 2.58 eV when using the B3LYP functional and HW+ ECP. A comparable value of 2.49 eV was obtained when using the SD ECP on Ta^{2+}. Holthausen et al.[39] have previously characterized the overbinding of the B3LYP functional for the comparable third-row transition metal ion methyl cations, which also involves a single covalent metal−ligand bond. These authors suggest using the BHLYP functional as an alternative, and indeed, we obtain lower bond energies of 2.30 (HW+) and 2.21 (SD) eV. At the QCISD(T) level of theory, we find a bond energy of 2.45 eV. Given this range of calculated BDEs, the formation of $TaH^{2+} + CH_3$ should

TABLE 2: Optimized Parameters for Eq 1 for Ta^{2+} + CH_4 and CD_4 Systems

	reaction	σ_0	n	E_0 (eV)	$D_0(Ta^{2+}\text{-}L)$ (eV)
$Ta^{2+}+CH_4$	$\rightarrow TaCH_3^{2+} + H$	0.41 ± 0.25	1.0 ± 0.1	1.10 ± 0.19	3.38 ± 0.19
	$\rightarrow TaCH_2^{2+} + H_2$			<0	>4.71
	$\rightarrow TaC^{2+} + 2\ H_2$	1.98 ± 0.33	0.9 ± 0.1	2.87 ± 0.20	5.19 ± 0.20
$Ta^{2+}+CD_4$	$\rightarrow TaCD_3^{2+} + D$	0.62 ± 0.12	0.9 ± 0.2	1.15 ± 0.27	3.43 ± 0.27
	$\rightarrow TaCD_2^{2+} + D_2$			<0	>4.82
	$\rightarrow TaC^{2+} + 2\ D_2$	4.13 ± 0.66	0.9 ± 0.1	2.72 ± 0.10	5.48 ± 0.10

TABLE 3: Experimental and Theoretical Bond Energies (eV) for $Ta^{2+}-H$ and $Ta^{2+}-CH_x$ ($x = 0-3$)

			B3LYP		BHLYP		QCISD(T)[a]
species	state	expt	HW+	SD	HW+	SD	HW+
$Ta^{2+}-H$	$^3\Sigma^-$		2.58	2.49	2.30	2.21	2.45
$Ta^{2+}-CH_3$	$^3A''$	3.40±0.16	4.21	3.99	3.54	3.34	4.35
$Ta^{2+}-CH_2$	$^2A'$	>4.71	5.68	5.47	4.83	4.64	5.83
$Ta^{2+}-CH$	$^1\Sigma^+$		6.51	7.00	5.53	5.31	5.99
$Ta^{2+}-C$	$^2\Sigma^+$	5.42±0.19	4.78	4.59	3.74	3.56	5.13

[a] Geometries calculated at the B3LYP/HW+/6−311++G(3df,3p) level of theory.

be endothermic by 1.9−2.3 eV, whereas charge separation to yield TaH^+ + CH_3^+ is exothermic by over 4 eV. Hence, the TaH^{2+} product is not formed because, as these products separate, an electron transfer can readily yield the lower energy TaH^+ + CH_3^+ product channel.

The ground state for TaH^{2+} is a $^3\Sigma^-$. This molecule has an electronic configuration of $\sigma_b{}^2(\delta/\pi)^2$, in which there is a covalent σ bond, σ_b, with two singly occupied nonbonding metal valence orbitals calculated to have mixed π and δ symmetries. At the B3LYP level of theory, this state is determined to have a bond length of 1.721 (HW+) and 1.733 (SD) Å, whereas at the BHLYP level of theory, the bond lengths are 1.710 (HW+) and 1.720 (SD) Å. The lowest lying excited state of TaH^{2+} is $^3\Phi$, lying 0.14 eV higher in energy and having a $\sigma_b{}^2\pi^1\delta^1$ configuration. Other excited states include $^3\Delta$ ($\sigma_b{}^2\delta^1\sigma^1$), $^1\Sigma^+$ ($\sigma_b{}^2(\delta/\pi)^2$), $^1\Phi$ ($\sigma_b{}^2\pi^1\delta^1$), $^3\Sigma^-$ ($\sigma_b{}^2(\pi/\delta)^2$), $^1\Delta$ ($\sigma_b{}^2\delta^1\sigma^1$), $^5\Delta$ ($\sigma_b{}^1\pi^2\delta^1$), and $^5\Sigma^-$ ($\sigma_b{}^1\pi^2\sigma^1$), where the higher lying σ orbital is largely 6s on the Ta. Relative energies of these states are listed in Table S1 and their geometries are given in Table S2, Supporting Information.

4.2. $Ta^{2+}-CH_3$. For the methane system, using eq 17 with $D_0(H-CH_3) = 4.48$ eV and our threshold value of 1.10 ± 0.19 eV (Table 2), we obtain a BDE for $TaCH_3^{2+}$ of 3.38 ± 0.19 eV. Similarly, with $D_0(D-CD_3) = 4.58$ eV and a threshold of 1.15 ± 0.27 eV, the bond energy derived from the CD_4 system for $TaCD_3^{2+}$ is 3.43 ± 0.27 eV. After correcting for zero point energy differences in these two values (−0.013 eV), we obtain a weighted average value of 3.40 ± 0.16 eV for the BDE of $Ta^{2+}-CH_3$.

For our theoretical calculations, Table 3, we find $D_0(Ta^{2+}-CH_3) = 4.21$ eV at the B3LYP (HW+) level of theory. Using the SD ECP, our predicted bond energy drops by 0.22 eV, yielding a value of 3.99 eV. With the BHLYP functional, however, there is a more substantial decrease in bond energy to 3.54 (HW+) and 3.34 (SD) eV, in reasonable agreement with experiment. The QCISD(T) calculations give the highest predicted value, 4.35 eV.

The ground state of $TaCH_3^{2+}$ is found to be $^3A''$ with C_s symmetry (Figure 3) and has a valence electronic configuration (using the analogous C_{3v} symmetry designations) of $1a_{1b}{}^2 1e_\delta{}^1 2a_1{}^1$, where the $1a_{1b}$ is the Ta−C σ bonding orbital, the $1e_\delta$ orbital is a 5d (δ-like) nonbonding orbital on Ta, and the $2a_1$ orbital is a nonbonding 6s5d hybrid orbital on Ta. The Ta−C and C−H bond lengths are 1.928, 1.096, and 1.150 (2) Å, and the TaCH bond angles are 86.0° (2) and 150.6°, as compared with the ground state of $TaCH_3^+$ ($^4A_1$), 2.058 Å, 1.098 Å (3), and 110.2° (3).[36] The first excited state, $^3A'$, is found to lie only 0.01 eV higher in energy (Table S1), which is consistent with the $1a_{1b}{}^2 1e_\delta{}^1 2a_1{}^1$ configuration that differs from the ground state only in which $1e_\delta$ orbital is occupied. In this state, the Ta−C bond length is slightly longer, 1.950 Å, whereas two of the C−H bond lengths are slightly shorter, 1.098 and 1.136 (2) Å, with somewhat less distortion from C_{3v} symmetry in that the TaCH bond angles are 93.1° (2) and 138.4°. $^3A_1$ (C_{3v}, $1a_{1b}{}^2 1e_\delta{}^1 e_\pi{}^1$) and $^1A_1$ (C_{3v}, $1a_{1b}{}^2 1e_\delta{}^1 e_\pi{}^1$) states lie 0.17 and 0.18 eV, respectively, above the ground state. Other excited states include $^1A''$ (C_s, $1a_{1b}{}^2 1e_\delta{}^2$), $^1A''$ (C_s, $1a_{1b}{}^2 1e_\delta{}^2$), $^1A'$ (C_s, $1a_{1b}{}^2 2a_1{}^2$), $^5A_1$ (C_{3v}, $1a_{1b}{}^1 1e_{\delta(\pi)}{}^2 2a_1{}^1$), and $^5A'$ (C_s, $1a_{1b}{}^1 1e_\pi{}^1 1e_\delta{}^1 2a_1{}^1$) lying 0.19, 0.45, 1.02, 1.49, and 1.54 eV, respectively, above the ground state, where the C_{3v} symmetry designations of the valence orbitals are used in all cases.

Theoretical bond energies for TaH^{2+} and $TaCH_3^{2+}$ indicate the latter is bound more strongly by 1.1−1.9 eV (Table 3). For the hydride, the single 1s electron on hydrogen can form only a single covalent bond, hence, theoretical bond energies for TaH^{2+} (2.30 eV) and TaH^+ (2.61 eV) at the BHLYP/HW+ level of theory are similar to one another. In contrast, the bond energy for $TaCH_3^{2+}$ (3.54 eV) is calculated to be much stronger than that for $TaCH_3^+$ (2.83 eV) (BHLYP/HW+ level of theory).[36] This difference can be attributed to the distortion of the molecule from C_{3v} symmetry (Figure 3). By tilting the methyl group, two C−H bonds begin to interact with the metal ion, resulting in

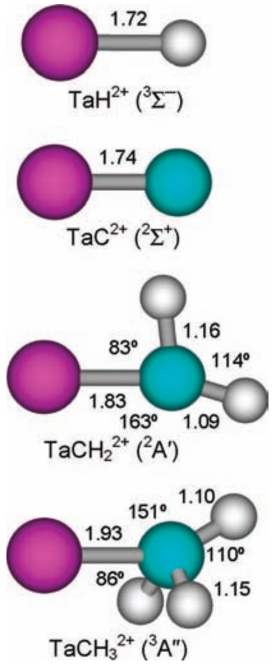

Figure 3. Structures of ground-state products calculated at the B3LYP/HW+/6−311++G(3df,3p) level of theory. Bond lengths are given in Å and HTaC and HCH bond angles are given in degrees.

an agostic interaction between the occupied CH_3 (b_1) bonding orbital and the empty in-plane 5dπ orbital on Ta.

We also investigated a number of alternate isomers of the $TaCH_3^{2+}$ molecule. The isomer having the lowest energy, 0.45 eV above $TaCH_3^{2+}$ ($^3A''$), is $HTaCH_2^{2+}$, which has a ^1A ground state. The H−Ta and Ta−C bond lengths and HTaC bond angle are 1.726 Å, 1.822 Å, and 99.0°, respectively, indicating that the Ta−H bond is a covalent single bond and the Ta−C bond is a covalent double bond. The $(H)_2TaCH^{2+}$ isomer was also located, 3.25 eV above $TaCH_3^{2+}$ ($^3A''$). The $^1A'$ ground state of this isomer has Ta−H bond lengths of 1.741 Å, suggesting covalent single bonds, and a Ta−C bond length of 1.926 Å, slightly longer than that of $TaCH_2^{2+}$ and much longer than that in $TaCH^{2+}$ (see below). Finally, there is also the $(H_2)TaCH^{2+}$ isomer, which has a $^1A'$ ground state, with a short Ta−C bond, 1.773 Å, comparable to that of $TaCH^{2+}$ ($^1\Sigma^+$); short Ta−H bonds, 1.916 and 1.932 Å; and a short H−H bond, 0.858 Å. This geometry is consistent with a tightly bound dihydrogen molecule bound to ground state $TaCH^{2+}$. Excited states of each of these isomers were also characterized; see Tables S1 and S2.

4.3. Ta^{2+}−CH_2. Reaction 5 and its perdeuterio analogue are exothermic which gives a lower limit for the bond dissociation energy of $TaCH_2^{2+}$ of 4.71 ± 0.03 eV = $D_0(CH_2{-}H_2)$ and $TaCD_2^{2+}$ of 4.82 ± 0.03 eV = $D_0(CD_2{-}D_2)$. Ranasinghe et al.[8] report a value of >4.81 eV from the same observation, using 298 K thermodynamic values.

The present calculations, B3LYP/HW+ (SD) and QCISD(T), find a $^2A'$ ground state with C_s symmetry (Figure 3) for $TaCH_2^{2+}$ with a bond energy of 5.68 (5.47) and 5.83 eV, respectively. The BHLYP/HW+ (SD) functional yields lower values, 4.83 (4.64) eV. We find that the $^2A'$ ground state of the $TaCH_2^{2+}$ molecule distorts from C_{2v} symmetry by bending in the plane of the molecule such that one C−H bonds interacts with the metal ion, in essence, an agostic interaction that allows the CH_2 ($1b_2$) doubly occupied bonding orbital in the plane of the molecule to donate into the empty Ta ($5d_{yz}$) orbital, given that the molecule lies in the *yz* plane with the Ta−C bond along the *z* axis. For our ground-state geometry, we obtain r(Ta−C) = 1.830 Å, r(C−H) = 1.094 and 1.163 Å, and ∠TaCH = 163.0° and 83.4° (Table S2). Our calculations also located several excited states (Table S1). The first four excited states, $^2A''$, $^4B_2$, $^4B_1$, and $^2B_1$, lie 0.13, 0.49, 0.52, and 0.76 eV higher in energy, respectively.

The $^2A'$ ground state of $TaCH_2^{2+}$ has a valence electronic configuration of (using the analogous C_{2v} symmetry designations) $(1a_{1b})^2(1b_{1b})^2(2a_1)^1$, where the $1a_{1b}$ and $1b_{1b}$ orbitals are the Ta−C σ and π bonding orbitals, and the $2a_1$ orbital is a nonbonding 6s−5dσ hybrid orbital on Ta. Thus, there is a covalent double bond between Ta^{2+} and CH_2. The $^2A''$, $^4B_2$, $^4B_1$, and $^2B_1$ excited states have valence electronic configurations of $(1a_{1b})^2(1b_{1b})^2(1a_2)^1$, $(1a_{1b})^2(1b_{1b})^1(2a_1)^1(1a_2)^1$, $(1a_{1b})^2(1b_{1b})^1(2a_1)^1(3a_1)^1$, and $(1a_{1b})^2(1b_{1b})^1(2a_1)^1(3a_1)^1$, respectively, where the $1a_2$ ($5d_{xy}$) and $3a_1$ ($5d_{x2-y2}$) orbitals are nonbonding orbitals on the tantalum.

It was verified that the $TaCH_2^{2+}$ isomer was the lowest energy arrangement of atoms. The lowest lying $HTaCH^{2+}$ isomer lies 1.63 eV higher in energy and has a $^2A''$ ground state. The Ta−C and C−H bond lengths in this molecule are 1.859 and 1.098 Å, respectively, with a HTaC bond angle of 89.8°. Other low lying states, $^2A'$ and $^6A'$, were found lying 2.97 and 4.04 eV higher in energy than ground state $TaCH_2^{2+}$.

4.4. Ta^{2+}−CH. As for TaH^{2+}, doubly charged $TaCH^{2+}$ was not observed experimentally, but theoretical results are included in Tables S1 and S2 for completeness. For Ta^{2+}−CH, we calculate bond dissociation energies of 5.3−7.0 eV at the various levels of theory considered; see Table 3. These values average about 15% greater than the calculated bond energies for $TaCH_2^{2+}$, consistent with an increase in the bond order. The ground state for $TaCH^{2+}$ is $^1\Sigma^+$, having a bond order of 3.0 with a valence electron orbital occupation of $1\sigma_b^2 1\pi_b^4$, where the $1\sigma_b$ and $1\pi_b$ orbitals are the obvious Ta−C bonding orbitals. The molecule is linear with Ta−C and C−H bond lengths of 1.759 and 1.096 Å, respectively. Several excited states were also located lying 0.51 eV and higher in energy; see Table S1. The alternate $HTaC^{2+}$ structure was also considered and found to lie 3.46 eV higher in energy than $TaCH^{2+}$ ($^1\Sigma^+$); see Table S1.

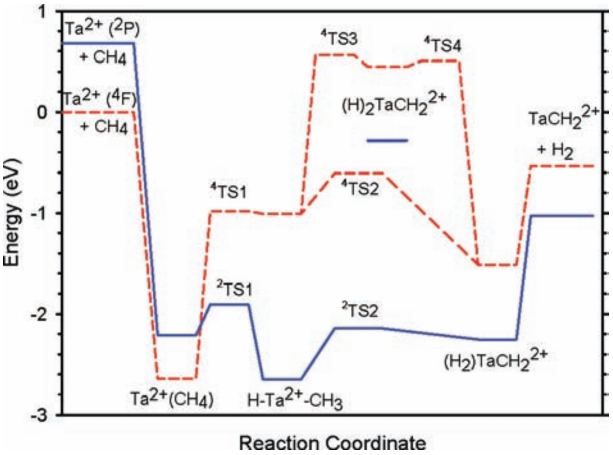

Figure 4. $[Ta,C,4H]^{2+}$ potential energy surfaces derived from theoretical results. The relative energies of all species are based on ab initio calculations at the B3LYP/HW+/6−311++G(3df,3p) level, Table S3, Supporting Information, relative to the Ta^{2+} (^4F) + CH_4 ground-state asymptote.

4.5. Ta^{2+}−C. Cross sections from the perprotiated and perdeuterated methane experiments provide thresholds of 2.87 ± 0.20 and 2.72 ± 0.10 eV for formation of TaC^{2+}, respectively. These thresholds correspond to BDEs of 5.19 ± 0.20 and 5.48 ± 0.10 eV (Table 2). Our best experimental value for $D_0(Ta^{2+}{-}C)$ is the weighted average of these two values, 5.42 ± 0.19 eV. This experimental value is in poor agreement with the results of the present calculations, 4.78 (B3LYP/HW+) and 4.59 (B3LYP/SD) eV; see Table 3. The BHLYP functional yields BDEs even further below experiment, 3.74 (HW+) and 3.56 (SD) eV, whereas the QCISD(T) performs better than the DFT methods, yielding a BDE of 5.13 eV.

We calculate the ground state for TaC^{2+} to be $^2\Sigma^+$ (Figure 3), having a bond order of 2.5. The valence electron orbital occupation is $1\sigma_b^1 1\pi_b^4$, where the $1\sigma_b$ and $1\pi_b$ orbitals are the obvious bonding orbitals. The lowest lying excited state is a $^4\Phi$, lying 0.54 eV higher in energy and has a $1\sigma_b^1 1\pi_b^3 1\delta^1$ configuration. Other stable excited states (no imaginary frequencies) include $^2\Phi$ ($1\sigma_b^1 1\pi_b^3 1\delta^1$), $^6\Delta$ ($1\sigma_b^1 1\pi_b^2 1\delta^1 2\sigma^1$), $^4\Delta$ ($1\sigma_b^1 1\pi_b^2 1\delta^1 2\sigma^1$), $1^2\Delta$ ($1\sigma_b^1 1\pi_b^2 1\delta^1 2\sigma^1$), $^61\Sigma^+$ ($1\sigma_b^1 1\pi_b^2 1\delta^2$), $^41\Sigma^-$ ($1\sigma_b^2 1\pi_b^2 2\sigma^1$), $^6\Phi$ ($\sigma_b^1 \pi_b^2 \delta^1 \pi^1$), and $^4\Phi$ ($1\sigma_b^1 1\pi_b^2 1\delta^1 2\pi^1$), Table S1, where the 1δ and 2σ orbitals are nonbonding 5d and 6s5d hybrid orbitals, respectively, on Ta, and the 2π is antibonding.

4.6. Potential Energy Surfaces of $[Ta,C,4H]^{2+}$. Figure 4 illustrates the potential energy surfaces (PES) for the interaction of Ta^{2+} with methane. The energies of all intermediates are listed in Table S3, and the geometric parameters of these species are provided in Table S4 and shown in Figures 5 (quartet states)

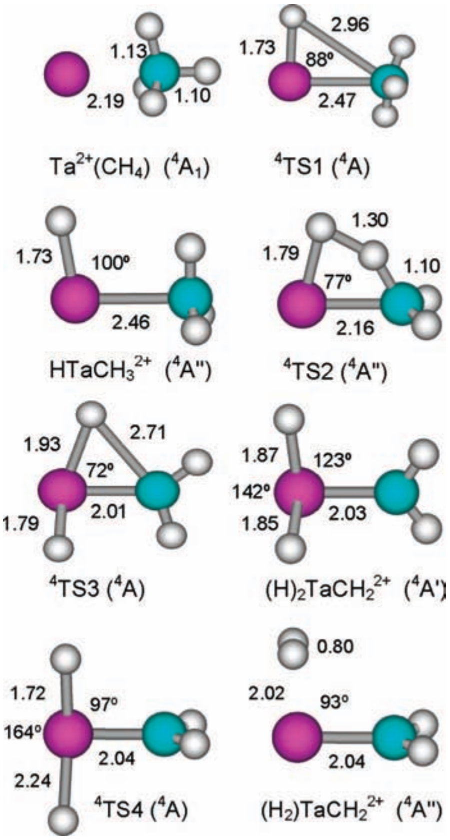

Figure 5. Structures of several intermediates and transition states along the quartet surface of the $[Ta,C,4H]^{2+}$ system calculated at the B3LYP/HW+/6−311++G(3df,3p) level of theory. Bond lengths are given in Å and HTaC and HTaH bond angles in degrees.

and 6 (doublet states). Calculations were performed at the B3LYP level of theory and include zero-point energy corrections (scaled by 0.989). Transition states were located using the synchronous transit-guided quasi-Newton method[48,49] followed by frequency calculations and geometry optimizations to verify a first-order saddle point. Calculations were also carried out for sextet states of the various species but, in all cases, are found to lie much higher in energy than the quartet and doublet states listed.

4.7. Quartet Surface. On the potential energy surface for interaction of Ta^{2+} (^4F) with methane (Figure 4) a $Ta^{2+}(CH_4)$ adduct, in which the methane molecule remains intact and largely unperturbed occurs, is initially formed. The methane molecule binds with C_{3v} symmetry and the complex has a $^4A_1$ ground state (Figure 5). The $Ta^{2+}-CH_4$ bond energy is 2.64 eV as compared with the Ta^+-CH_4 (^5A) bond energy of 0.56 eV.[36] Likewise, the Ta−C bond distance in $Ta^{2+}-CH_4$ of 2.188 Å is much shorter than that in Ta^+-CH_4, 2.626 Å.[36] Not surprisingly, the extra charge on Ta provides much tighter binding for this noncovalent complex.

As the Ta−H bond distance reduces, the system passes over a transition state, ^{4}TS1, which lies 0.98 eV below the energy of the reactants, leading to the $H-Ta^{2+}-CH_3$ insertion intermediate. This transition state has C_1 symmetry (^4A) and a H−Ta−C bond angle of 87.8° (Figure 5). On the quartet surface, the $HTaCH_3^{2+}$ intermediate has C_s symmetry ($^4A''$) and has a H−Ta−C bond angle of 99.8°. The Ta−H bond distance is 1.726 Å, as compared with that of ground state $Ta^{2+}-H$ ($^3\Sigma^-$), 1.721 Å. The Ta−C bond distance is relatively long, 2.464 Å, compared with the Ta−C bond distance in ground state $TaCH_3^{2+}$ ($^3A''$) of 1.928 Å. Furthermore, the average HCH bond angle in the methyl group of $TaCH_3^{2+}$ ($^3A''$) is 109° versus that for a free CH_3 radical of 120°, whereas the $HTa^{2+}-CH_3$ intermediate has an average HCH bond angle of 119° in the methyl group. These observations indicate that the methyl group is not covalently bound to the TaH^{2+} molecule in this spin state. From this intermediate, $HTa^{2+}-CH_3$ and $CH_3Ta^{2+}-H$ bond energies are theoretically determined to be 2.83 and 1.20 eV, respectively.

From $HTaCH_3^{2+}$ ($^4A''$), the system can proceed directly to a $(H_2)TaCH_2^+$ intermediate via a four-center transition state, ^{4}TS2, which lies 0.61 eV below the reactants energy. This transition state has C_s symmetry, $^4A''$ state (Figure 5), and the Ta−C bond distance is 2.156 Å. The $(H_2)TaCH_2^{2+}$ intermediate ($^4A''$) has a Ta−C bond distance of 2.045 Å, as compared to the Ta−C bond distance in the lowest lying quartet state $TaCH_2^{2+}$ ($^4B_2$) of 2.039 Å. The C−H bond distances are 1.100 (2) Å for $(H_2)TaCH_2^{2+}$ ($^4A''$) and 1.103 (2) Å for $TaCH_2^{2+}$ ($^4B_2$). The H−H bond distance is 0.802 Å compared to free H_2 at 0.742 Å. The $H_2CTa^{2+}-H_2$ bond energy is calculated to be 1.02 eV. Overall, formation of $TaCH_2^{2+} + H_2$ along this pathway is calculated to be exothermic by 0.54 eV, with no barriers in excess of the reactants (Figure 4), consistent with the experimental data for reaction 5.

Alternatively, the $HTaCH_3^{2+}$ ($^4A''$) intermediate can follow a stepwise pathway involving sequential H atom transfer to form a $(H)_2TaCH_2^{2+}$ ($^4A'$) dihydride intermediate (Figure 5). The Ta−C bond distance is 2.030 Å, which is comparable to the Ta−C bond distance in the lowest lying quartet state of $TaCH_2^{2+}$ ($^4B_2$), 2.039 Å. The dihydride intermediate, lying 0.45 eV above reactants, is reached via ^{4}TS3, which lies 0.56 eV above the reactants. Continuing along the quartet surface, the dihydride intermediate can reductively eliminate the H_2 molecule, carrying the molecule across ^{4}TS4, which lies 0.50 eV above the reactants. Clearly, this stepwise reaction pathway is too high in energy to be consistent with the observed exothermic and barrierless production of $TaCH_2^{2+} + H_2$ in reaction 5.

4.8. Doublet Surface. Reaction of methane with doublet state Ta^{2+} (^2P) leads initially to the formation of a $Ta^{2+}(CH_4)$ adduct in a $^2A'$ state (C_s symmetry), Figure 6. On the doublet surface, $Ta^{2+}(CH_4)$, lies 2.21 eV below the ground-state reactant asymptote and 0.43 eV above $Ta^{2+}(CH_4)$ ($^4A''$), somewhat less than the calculated $^4F - {}^2P$ atomic excitation energy of 0.68 eV. As the Ta−H bond distance decreases, the system passes over ^{2}TS1, leading to the $H-Ta^{2+}-CH_3$ (^2A) insertion intermediate. This transition state has C_1 symmetry (^2A) and a H−Ta−C bond angle of 46.8° (Figure 6). The $HTaCH_3^{2+}$ (^2A) intermediate has a H−Ta−C bond angle of 98.2°, with a Ta−H bond distance, 1.723 Å, that is similar to ground state TaH^{2+}, 1.721 Å. The Ta−C bond distance, 1.934 Å, is also similar to the Ta−C bond distance in $TaCH_3^{2+}$ ($^3A''$), 1.928 Å. This observation indicates that the hydrogen atom and methyl group are covalently bound to Ta^{2+} in this spin state. The $HTa^{2+}-CH_3$ and $H-TaCH_3^{2+}$ bond energies are calculated to be 4.47 and 2.84 eV, respectively. This is consistent with the relative bond energies of $TaCH_3^{2+}$ and TaH^{2+} listed in Table 3.

Continuing along the doublet surface, the system can proceed from $HTaCH_3^{2+}$ (^2A) directly to a $(H_2)TaCH_2^{2+}$ intermediate via a four-center transition state, ^{2}TS2. This ^2A transition state has C_1 symmetry with a Ta−C bond distance of 1.869 Å, indicating that the CH_2 group is quite tightly bound. This Ta−C bond distance is slightly longer than that in ground-state $TaCH_2^{2+}$ ($^2A'$), 1.830 Å. ^{2}TS2 leads to a $(H_2)TaCH_2^{2+}$ intermediate (^2A) that has a similar geometry to $TaCH_2^{2+}$ ($^2A'$), with a Ta−C bond distance of 1.844 Å, clearly indicating a double bond. The C−H bond distances are 1.093 and 1.157 Å for

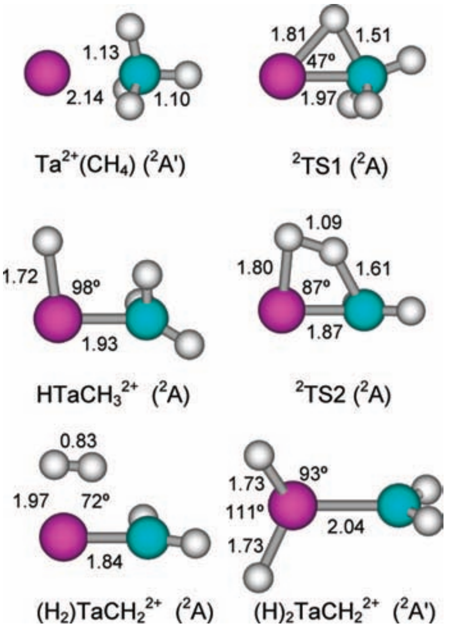

Figure 6. Structures of several intermediates and transition states along the doublet surface of the $[Ta,C,4H]^{2+}$ system calculated at the B3LYP/HW+/6−311++G(3df,3p) level of theory. Bond lengths are given in Å and HTaC and HTaH bond angles in degrees.

$(H_2)TaCH_2^{2+}$ (^2A) compared with 1.094 and 1.163 Å for ground state $TaCH_2^{2+}$ ($^2A'$). The $TaCH_2^+-H_2$ bond dissociation energy is 1.23 eV and the H−H bond distance is 0.827 Å, somewhat longer than that calculated for free H_2, 0.742 Å. Overall, formation of $TaCH_2^{2+}$ ($^2A'$) + H_2 is exothermic by 1.03 eV from ground state Ta^{2+} (^4F) + CH_4 reactants.

We carefully looked for a stepwise pathway on the doublet surface and although a dihydrido tantalum carbene dication intermediate was located (Figure 6) searches for the transition states on either side of this species (^{2}TS3 and ^{2}TS4) always collapsed to the lower energy doublet surface for the concerted pathway. This behavior is not surprising given that the energy of this intermediate lies 2.37 eV above the global minimum (only 0.28 eV below ground-state reactants).

5. Discussion

5.1. σ−Bond Activation. In our previous studies,[20,30−32,34,36,50−57] the activation of methane by atomic metal ions has been explained using a simple donor−acceptor model, leading to an oxidative addition mechanism.[41,42] σ bond activation at a metal center requires an electronic configuration in which there is an empty acceptor orbital on the metal ion into which the electrons of a bond to be broken are donated. In tandem, metal electrons in orbitals having π-like symmetry back-donate into the antibonding orbital of the bond to be broken. If the acceptor orbital is occupied, a repulsive interaction can result leading to inefficient reaction either by introduction of a barrier to the reaction or by more direct abstraction pathways. For Ta^{2+}, both the ^4F and the ^2P states have an unoccupied 6s acceptor orbital. Oxidative addition of a C−H bond to M^{2+} forms a $H-M^{2+}-CH_3$ intermediate in such a mechanism and products can be formed by the reductive elimination of H_2 at low energies and by further dehydrogenation of primary products at still higher energies. For first-row transition metal ions, the reductive elimination process occurs through a four-centered transition state from the $H-M^+-CH_3$ intermediate to a $(H_2)MCH_2^+$ intermediate, in which molecular hydrogen is electrostatically bound to the MCH_2^+ species.[50,53,55,56] The $(H_2)MCH_2^+$ intermediate then decomposes by expulsion of H_2. This pathway is also the lowest energy channel for the third-row transition metal ions, Hf^+ and Ta^+.[34,36] For other third-row transition metal ions, W^+,[32] Re^+,[31] Ir^+,[57] and Pt^+,[30] a different reaction mechanism involving a dihydride methylene intermediate has been confirmed by calculations.

5.2. Mechanism for Dehydrogenation of Methane by Ta^{2+}. Ground state Ta^{2+} (^4F, $5d^3$) forms a $TaCH_4^{2+}$ ($^4A_1$) adduct upon interaction with CH_4. This intermediate can then move along the quartet surface passing over ^{4}TS1 to form the hydrido tantalum methyl dication intermediate, $H-Ta^{2+}-CH_3$ ($^4A''$). Note that this transition state is quite late, such that its geometry and energy are similar to the tantalum dication hydrido methyl intermediate; see Figures 4 and 5. Next, the $H-Ta^{2+}-CH_3$ intermediate can follow a concerted pathway for producing $(H_2)TaCH_2^{2+}$ ($^4A''$), which easily loses dihydrogen to form $TaCH_2^{2+}$ ($^4B_2$) + H_2 products. This pathway involves a four-centered transition state, ^{4}TS2, which leads directly between these two intermediates. The energy-limiting step is the final expulsion of H_2, and all transition states and intermediates lie below the energy of the reactants, Figure 4, consistent with the barrierless process observed experimentally.

Although the quartet surface is low in energy, the lowest energy pathway for dehydrogenation involves coupling to the doublet surface during the C−H bond activation step; see Figure 4. This forms ^{2}TS1, which is a much earlier transition state than ^{4}TS1; see Figures 4 and 6. From ^{2}TS1, the hydrido tantalum methyl dication intermediate, $H-Ta^{2+}-CH_3$ (^2A), is reached. Because this spin state allows formation of two covalent bonds using 6s5d hybrid orbitals, this intermediate is much lower in energy than its quartet analogue and is the global minimum on the potential energy surface. Next, the $H-Ta^{2+}-CH_3$ intermediate can follow a concerted pathway for producing $(H_2)TaCH_2^{2+}$ (^2A) that involves a four-centered transition state, ^{2}TS2. The $(H_2)TaCH_2^{2+}$ (^2A) intermediate easily loses dihydrogen and leads directly to ground state $TaCH_2^{2+}$ ($^2A'$) + H_2 products.

In analogy with other third-row transition metal cations, we also looked for a second pathway entailing the activation of a second C−H bond (α−H transfer), leading to the formation of dihydrido methylene tantalum dication intermediates. On the quartet surface, activation of the second C−H bond involves ^{4}TS3 and forms $(H)_2Ta^{2+}CH_2$ ($^4A'$). From this intermediate, reductive elimination of the dihydrogen molecule passes over ^{4}TS4 and leads again to $(H_2)Ta^{2+}CH_2$ ($^4A''$). All three of these species lie quite high in energy with a rate-limiting transition state of ^{4}TS3 at 0.56 eV above reactants; see Figure 4. Thus, this pathway is not experimentally viable. On the doublet surface, we could locate an analogous dihydride methylene intermediate, $(H)_2Ta^{2+}CH_2$ ($^2A'$), but this species also lies quite high in energy, only 0.28 eV below reactants and well-above the concerted pathway. In this case, searches for ^{2}TS3 and ^{2}TS4 always collapsed to the much lower energy concerted surface.

5.3. Mechanism for Other Product Channels. The observation of $TaH^+ + CH_3^+$ and $TaCH_3^{2+}$ + H product channels are easily explained by simple metal−ligand bond cleavages from the $H-Ta^{2+}-CH_3$ intermediates. Indeed, observation of these channels support the formation of a $H-Ta^{2+}-CH_3$ intermediate in the mechanism proposed above. Charge transfer to form $Ta^+ + CH_4^+$ is an exothermic reaction that could conceivably occur either at long-range by electron transfer or by proceeding through an intermediate like the $Ta^{2+}(CH_4)$ complex.

At higher energies, TaC^{2+} is observed and can be attributed to dehydrogenation of the $TaCH_2^{2+}$ primary product. The

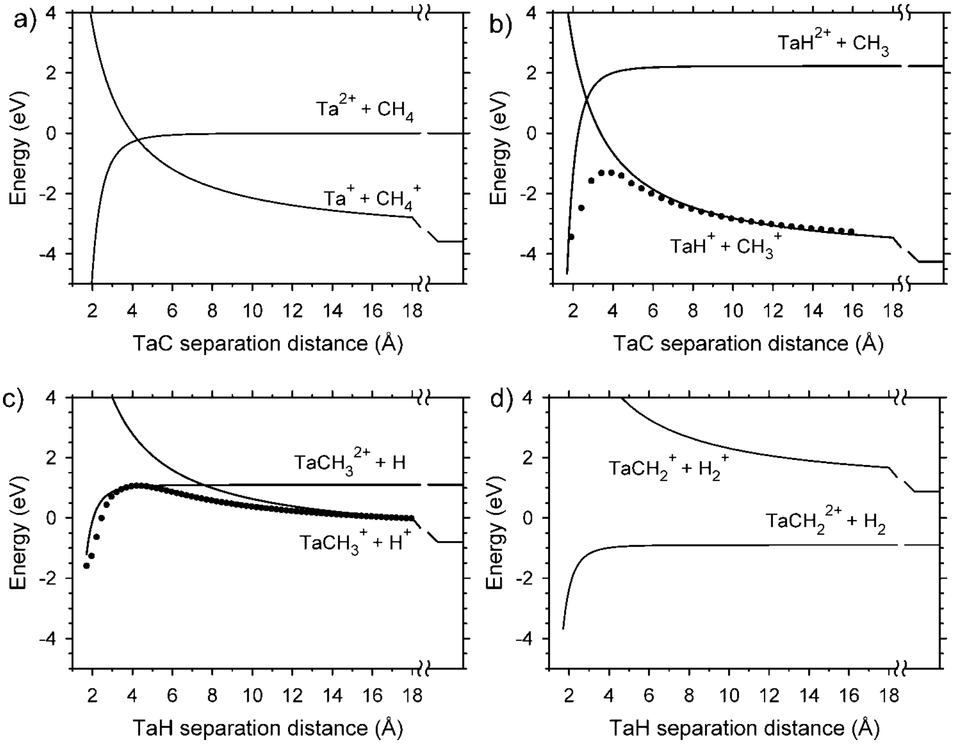

Figure 7. Curve crossing model derived from experimental data (full lines) and theoretical results calculated at a B3LYP/HW+/6−311++G(3df,3p) level of theory (symbols). The relative energies of the $TaH^+ + CH_3^+$ (part b) and $TaCH_3^+ + H^+$ (part c) theoretical curves have been adjusted so that the asymptotic energies agree with experimental values, hence the potential wells do not match the theoretical value of −2.65 eV.

coupling between these two products is demonstrated by the fact that the cross section for $TaCH_2^{2+}$ decreases as that for TaC^{2+} rises. Finally, as noted above, the formation of the $TaCH_3^+$ product ion can be attributed to hydride transfer between $TaCH_2^{2+}$ and CH_4 in a secondary collision.

5.4. Curve Crossing Model. Curve-crossing models have proven to provide considerable insight into the reaction of doubly charged metal cations with alkanes and help explain the branching between C−H bond activation, charge separation, and charge transfer reactions.[5−8] Figure 7 shows the potential energy surfaces involved in such a curve-crossing model for the case of $Ta^{2+} + CH_4$. In the entrance channel corresponding to $Ta^{2+} + CH_4$ ($\Delta H = 0$), Figure 7a, the potential energy surface exhibits an attractive ion-induced dipole potential, $V(r) = -\alpha q^2/8\pi\epsilon_0 r^4 + \Delta H$, where α is the polarizability volume of the neutral reagent (2.56 Å^3),[47] $q = 2e$ is the charge on Ta, e is the charge of an electron, ϵ_0 is the permittivity of vacuum, r is the internuclear distance between Ta and C, and ΔH is the reaction endothermicity. In the other parts of Figure 7, the surfaces for doubly charged products have similar potentials with variations in the polarizability volumes of the neutral (0.67 Å^3 for H,[58] 0.81 Å^3 for H_2,[47] and an estimate of 2.0 Å^3 for CH_3), and the asymptotic energies (ΔH). Here, the reaction endothermicities are 2.2 eV for $TaH^{2+} + CH_3$ using $D_0(Ta^{2+}-H) = 2.3$ eV (from theory, Table 3), 1.1 ± 0.2 eV for $TaCH_3^{2+} + H$ using $D_0(Ta^{2+}-CH_3) = 3.40 \pm 0.16$ eV (Table 3), and 0.9 eV for $TaCH_2^{2+} + H_2$ using $D_0(Ta^{2+}-CH_2) = 5.6$ eV (from theory, Table 3). (It might be noted that, in previous examinations of such curve crossing models,[5−8] the only doubly charged surface considered was that of the reactants, i.e., that in Figure 7a. Technically, this ignores the fact that all other reaction channels are located along different reaction coordinates of the overall potential energy surface. So for instance, the surface for $TaH^+ + CH_3^+$ cannot possibly cross that for $Ta^{2+} + CH_4$ as one hydrogen atom is not physically in the same position.) For the charge transfer and charge separation products shown in Figure 7, the ion−ion repulsive potentials correspond to $V(r) = q^2/4\pi\epsilon_0 r + \Delta H$, where $q = e$ is the charge on each product, and the ΔH values are −3.6 ± 0.5 eV for reaction 2, −4.3 ± 0.5 eV for reaction 3, −0.8 ± 0.5 eV for reaction 14, and −0.9 ± 0.5 eV for reaction 15.

According to these surfaces, the attractive ion-induced dipole potential curve between the reactant ground state Ta^{2+} ion and the CH_4 neutral is crossed by the Coulombic repulsive curve for the $Ta^+ + CH_4^+$ products at 4.3 ± 0.6 Å at an energy of −0.2 ± 0.4 eV (Figure 7a). Thus, the rate limiting transition state for reaction 2, which occurs at the curve crossing, is nearly thermoneutral, which helps explain the relatively flat energy dependence observed for this reaction. An additional consideration is that the Franck−Condon factors for ionization of methane are small at the ground-state geometry of CH_4, such that CH_4^+ is distorted significantly from this geometry. Consequently, the two curves shown in Figure 7a are displaced from one another along a distortion coordinate in another dimension. This moves the true crossing point between these two surfaces to larger TaC separations at energies even closer to zero. The relevant potential surfaces for reaction 3 are shown in Figure 7b. Here, the potential for the $TaH^+ + CH_3^+$ products cross that for $TaH^{2+} + CH_3$ at 2.7 ± 0.2 Å and an energy of 1.1 ± 0.3 eV. Quantum chemical calculations of this surface at the B3LYP/HW+/6−311++G(3df,3p) level (a relaxed potential energy surface scan of the HTa−CH_3 bond distance) are also shown in Figure 7b after normalizing the calculated energy to the correct asymptotic energy. These calculations indicate that the curve crossing is strongly avoided, leaving a transition state at about −1.31 eV and $r = 3.7$ Å. Thus, this reaction occurs efficiently from the H−Ta^{2+}−CH_3 intermediate upon cleavage of the Ta−C bond.

In contrast to the behavior of reactions 2 and 3, the potential for the $TaCH_3^+ + H^+$ products (exothermic by 0.8 ± 0.5 eV) crosses that for $TaCH_3^{2+} + H$ (endothermic by 1.1 ± 0.2 eV) at a much larger distance of 7.6 +3.1/−1.7 Å at an energy of 1.1 ± 0.5 eV. Here, the surfaces are much more parallel, such that the avoided crossing does not drop the energy of the transition state appreciably. Indeed, quantum chemical calculations for this surface (a relaxed potential energy surface scan of the $H-TaCH_3$ bond distance) find the transition state lies at 1.13 eV and $r = 4.1$ Å, essentially matching the energy of the $TaCH_3^{2+} + H$ asymptote (Figure 7c). As a consequence, reaction 14 to form $TaCH_3^+ + H^+$ is not observed, but reaction 4 yielding $TaCH_3^{2+} + H$ is observed as an endothermic process (Figure 1a). This is presumably because the curve crossing occurs at a sufficiently long range that the electron transfer needed to move from the $TaCH_3^{2+} + H$ surface to the $TaCH_3^+ + H^+$ surface is inefficient.

For reaction 5, we note that the potential surface for $TaCH_2^{2+} + H_2$ does not cross that for $TaCH_2^+ + H_2^+$ because of the endothermicity of the latter channel (Figure 7d). Hence, there is no opportunity for the charge separation to occur along this reaction coordinate. Finally, we consider reaction 8, which could conceivably make $TaCH_3^{2+} + CH_3$ instead. Here, the $TaCH_3^+ + CH_3^+$ channel is exothermic by <4.6 ± 0.5 eV, whereas the charge retention channel is endothermic by more than 1.1 ± 0.2 eV, such that the curve crossing between these surfaces occurs at 2.9 ± 0.3 Å at an energy of 0.3 ± 1.0 eV. These results are consistent with observation of reaction 8.

Overall, the behavior of the various possible reaction channels corresponds well to the "reaction window" proposed by Lindinger and co-workers.[59] They suggested that charge transfer and charge separation reactions that occur via a curve crossing are favored when the crossing point ranges from internuclear separations of 2−6 Å. As noted above, this is true for reactions 2 and 3 (Figure 7a,b) and reaction 8, where the singly charged product channels are observed, but not the doubly charged analogues. In contrast, for reactions 4 and 5, the curve crossings occur outside this window (Figure 7c,d), such that the doubly charged products are observed, but not the singly charged analogues.

6. Conclusion

Ground state Ta^{2+} ions are found to be highly reactive with methane over a wide range of kinetic energies. At low energies, dehydrogenation is efficient, exothermic, and a dominant process over the product spectrum. Formation of $TaH^+ + CH_3^+$ and $Ta^+ + CH_4^+$ are also observed at low energies in exothermic processes. At higher energies, the $TaCH_2^{2+}$ product decomposes by loss of H_2 to form TaC^{2+} and $TaCH_3^{2+} + H$ is also formed. Several secondary processes (reactions 7−10) are also observed at low energies.

Analyses of the kinetic energy dependences of the reaction cross sections provide the BDEs of $Ta^{2+}-CH_3$ and $Ta^{2+}-C$, the first covalent bond energies measured to a metal dication. Our experimental BDE for $Ta^{2+}-CH_3$ is found to be in good agreement with ab initio calculations performed at the BHLYP/HW+/6−311++G(3df,3p) level of theory, and that for $Ta^{2+}-C$ is found to be in reasonable agreement with ab initio calculations performed at the QCISD(T)/HW+ level of theory (Table 3).

Calculations also provide a detailed potential energy surface for the $TaCH_4^{2+}$ system. When following the lowest energy pathway, the potential energy surface shows that the reaction of Ta^{2+} (^4F) with methane couples to a doublet surface near ^{2}TS1, followed by the oxidative addition of one C−H bond to yield a hydrido-methyl tantalum dication intermediate, $H-Ta^{2+}-CH_3$ (^2A), the global minimum on the potential energy surface. In the dominant process observed experimentally, the $H-Ta^{2+}-CH_3$ intermediate follows a concerted pathway involving a four-centered transition state (^{2}TS2) to form the electrostatic complex, $(H_2)TaCH_2^{2+}$ (^2A). Finally, H_2 is eliminated from $(H_2)TaCH_2^{2+}$ (^2A) to form the metal carbene complex, $TaCH_2^{2+}$ ($^2A'$) + H_2. The tantalum carbene retains the +2 charge as the separation to $TaCH_2^+ + H_2^+$ requires too much energy (Figure 7d). Overall, dehydrogenation of methane by Ta^{2+} has one spin change as it moves along the lowest energy pathway: Ta^{2+} (^4F) + CH_4 ($^1A_1$) → $Ta^{2+}(CH_4)$ ($^4A_1$) → $H-Ta^{2+}-CH_3$ (^2A) → $(H_2)TaCH_2^{2+}$ (^2A) → $TaCH_2^{2+}$ ($^2A'$) + H_2 ($^1\Sigma_g^+$). However, a comparable pathway on the quartet surface is available and also has no transition states in excess of the energy of the reactants, consistent with experimental observations.

The dehydrogenation reaction is found to occur with relatively high efficiency (47 ± 14%). In the present system, the reaction efficiency is not higher because charge separation channels forming $TaH^+ + CH_3^+$ account for another 22 ± 5% of the overall reactivity. This product channel can be formed by simple bond cleavage from the $H-Ta^{2+}-CH_3$ intermediate (doublet or quartet spin) and is an exothermic process with a low energy Coulombic barrier (Figure 7b). At higher energies, this intermediate can also decompose to form $TaCH_3^{2+} + H$ in an endothermic process. Formation of $TaCH_3^+ + H^+$, although exothermic, is suppressed by the Coulombic barrier along this reaction pathway (Figure 7c). Instead, the observed formation of $TaCH_3^+$ is attributed to the secondary reaction of $TaCH_2^{2+}$ with methane, where charge separation into $TaCH_3^+ + CH_3^+$ is facile. Exothermic charge transfer to form $Ta^+ + CH_4^+$ is also observed but is relatively inefficient, ~1% reactivity. This is consistent with a Coulombic barrier that is calculated to be near thermoneutral (Figure 7a).

Acknowledgment. Dedicated to Professor Helmut Schwarz on the occasion of his 65th birthday and in recognition of his many contributions to ion chemistry and understanding alkane bond activation by transition metals using mass spectrometic approaches. This work is supported by the National Science Foundation, Grant CHE-0748790. A grant of computer time from the Center for High Performance Computing in University of Utah is gratefully acknowledged. P.B.A. thanks Kent M. Ervin for reminding him about the interesting Franck−Condon aspects of Figure 7.

Supporting Information Available: Four tables (S1 − S4) containing energies and structures of the various reactants, products, intermediates, and transition states in the $[Ta,C,4H]^{2+}$ system. These materials are available free of charge via the Internet at http://pubs.acs.org.

References and Notes

(1) Schröder, D.; Schwarz, H. *J. Phys. Chem. A* **1999**, *103*, 7385–7394.
(2) Price, S. D. *Phys. Chem. Chem. Phys.* **2003**, *5*, 1717–1729.
(3) Mathur, D. *Phys. Rep.* **2004**, *391*, 1–118.
(4) Price, S. D. *Int. J. Mass Spectrom.* **2007**, *260*, 1–19.
(5) Tonkyn, R.; Weisshaar, J. C. *J. Am. Chem. Soc.* **1986**, *108*, 7128–7130.
(6) Buckner, S. W.; Freiser, B. S. *J. Am. Chem. Soc.* **1987**, *109*, 1247–1248.
(7) Gord, J. R.; Freiser, B. S.; Buckner, S. W. *J. Chem. Phys.* **1989**, *91*, 7530–7536.
(8) Ranasinghe, Y. A.; MacMahon, T. J.; Freiser, B. S. *J. Phys. Chem.* **1991**, *95*, 7721–7726.
(9) Ranasinghe, Y. A.; MacMahon, T. J.; Freiser, B. S. *J. Am. Chem. Soc.* **1992**, *114*, 9112–9118.

(10) Loh, S. K.; Hales, D. A.; Lian, L.; Armentrout, P. B. *J. Chem. Phys.* **1989**, *90*, 5466–5485.

(11) Teloy, E.; Gerlich, D. *Chem. Phys.* **1974**, *4*, 417–427.

(12) Gerlich, D. *Adv. Chem. Phys.* **1992**, *82*, 1–176.

(13) Ervin, K. M.; Armentrout, P. B. *J. Chem. Phys.* **1985**, *83*, 166–189.

(14) Chantry, P. J. *J. Chem. Phys.* **1971**, *55*, 2746–2759.

(15) Lifshitz, C.; Wu, R. L. C.; Tiernan, T. O.; Terwilliger, D. T. *J. Chem. Phys.* **1978**, *68*, 247–260.

(16) Kickel, B. L.; Armentrout, P. B. *J. Am. Chem. Soc.* **1995**, *117*, 4057–4070.

(17) Clemmer, D. E.; Chen, Y.-M.; Khan, F. A.; Armentrout, P. B. *J. Phys. Chem.* **1994**, *98*, 6522–6529.

(18) Haynes, C. L.; Armentrout, P. B. *Organometallics* **1994**, *13*, 3480–3490.

(19) Kickel, B. L.; Armentrout, P. B. *J. Am. Chem. Soc.* **1995**, *117*, 764–773.

(20) Chen, Y.-M.; Elkind, J. L.; Armentrout, P. B. *J. Phys. Chem.* **1995**, *99*, 10438–10445.

(21) Sievers, M. R.; Chen, Y.-M.; Elkind, J. L.; Armentrout, P. B. *J. Phys. Chem.* **1996**, *100*, 54–62.

(22) Azarov, V. I.; Tchang-Brillet, W.-U. L.; Qyart, J.-F.; Meijer, F. G. *Phys. Scr.* **2003**, *67*, 190–207.

(23) Chesnavich, W. J.; Bowers, M. T. *J. Phys. Chem.* **1979**, *83*, 900–905.

(24) Aristov, N.; Armentrout, P. B. *J. Am. Chem. Soc.* **1986**, *108*, 1806–1819.

(25) Armentrout, P. B. In *Advances in Gas Phase Ion Chemistry*; Adams, N. G., Babcock, L. M., Eds.; JAI Press: Greenwich, 1992; Vol. 1, pp 83−119..

(26) Shimanouchi, T. *NSRDS-NBS* 1972, *39*, 1.

(27) Becke, A. D. *J. Chem. Phys.* **1993**, *98*, 5648–5652.

(28) Lee, C.; Yang, W.; Parr, R. G. *Phys. Rev. B* **1988**, *37*, 785–789.

(29) Frisch, M. J.; Trucks, G. W.; Schlegel, H. B.; Scuseria, G. E.; Robb, M. A.; Cheeseman, J. R.; Montgomery, J. J. A.; Vreven, T.; Kudin, K. N. ; Burant, J. C.; Millam, J. M.; Iyengar, S. S.; Tomasi, J.; Barone, V.; Mennucci, B.; Cossi, M.; Scalmani, G.; Rega, N.; Petersson, G. A.; Nakatsuji, H.; Hada, M.; Ehara, M.; Toyota, K.; Fukuda, R.; Hasegawa, J.; Ishida, M.; Nakajima, T.; Honda, Y.; Kitao, O.; Nakai, H.; Klene, M.; Li, X.; Knox, J. E.; Hratchian, H. P.; Cross, J. B.; Adamo, C.; Jaramillo, J.; Gomperts, R.; Stratmann, R. E.; Yazyev, O.; Austin, A. J.; Cammi, R.; Pomelli, C.; Ochterski, J. W.; Ayala, P. Y.; Morokuma, K.; Voth, G. A.; Salvador, P.; Dannenberg, J. J.; Zakrzewski, V. G.; Dapprich, S.; Daniels, A. D.; Strain, M. C.; Farkas, O.; Malick, D. K.; Rabuck, A. D.; Raghavachari, K.; Foresman, J. B.; Ortiz, J. V.; Cui, Q.; Baboul, A. G.; Clifford, S.; Cioslowski, J.; Stefanov, B. B.; Liu, G.; Liashenko, A.; Piskorz, P.; Komaromi, I.; Martin, R. L.; Fox, D. J.; Keith, T.; Al-Laham, M. A.; Peng, C. Y.; Nanayakkara, A.; Challacombe, M.; Gill, P. M. W.; Johnson, B.; Chen, W.; Wong, M. W.; Gonzalez, C.; Pople, J. A. *Gaussian 03, Revision B.02*, Gaussian, Inc.: Pittsburgh, PA., 2003.

(30) Zhang, X.-G.; Liyanage, R.; Armentrout, P. B. *J. Am. Chem. Soc.* **2001**, *123*, 5563–5575.

(31) Armentrout, M. M.; Li, F.-X.; Armentrout, P. B. *J. Phys. Chem. A* **2004**, *108*, 9660–9672.

(32) Armentrout, P. B.; Shin, S.; Liyanage, R. *J. Phys. Chem. A* **2006**, *110*, 1242–1260.

(33) Li, F.-X.; Zhang, X.-G.; Armentrout, P. B. *J. Phys. Chem. A* **2005**, *109*, 8350–8357.

(34) Parke, L. G.; Hinton, C. S.; Armentrout, P. B *Int. J. Mass Spectrom.* **2006**, *254*, 168–182.

(35) Li, F.-X.; Armentrout, P. B. *J. Chem. Phys.* **2006**, *125*, 133114.

(36) Parke, L. G.; Hinton, C. S.; Armentrout, P. B. *J. Phys. Chem. C* **2007**, *111*, 17773–17787.

(37) Hay, P. J.; Wadt, W. R. *J. Chem. Phys.* **1985**, *82*, 299–310.

(38) Ohanessian, G.; Brusich, M. J.; Goddard III, W. A. *J. Am. Chem. Soc.* **1990**, *112*, 7179–7189.

(39) Holthausen, M. C.; Heinemann, C.; Cornehl, H. H.; Koch, W.; Schwarz, H. *J. Chem. Phys.* **1995**, *102*, 4931.

(40) Holthausen, M. C.; Mohr, M.; Koch, W. *Chem. Phys. Lett.* **1995**, *240*, 245.

(41) Armentrout, P. B.; Kickel, B. L. In *Organometallic Ion Chemistry;* Freiser, B. S., Ed.; Kluwer: Dordrecht, 1996; pp 1−45..

(42) Armentrout, P. B. In *Topics in Organometallic Chemistry;* Brown, J. M., Hofmann, P., Eds.; Springer-Verlag: Berlin, 1999; Vol. 4, pp 1−45..

(43) Andrae, D.; Haeussermann, U.; Dolg, M.; Stoll, H.; Preuss, H. *Theor. Chim. Acta* **1990**, *77*, 123–141.

(44) Moore, C. E. *Atomic Energy Levels, NSRDS-NBS 35*, Washington, D. C., 1971; Vol. III.

(45) Lias, S. G.; Bartmess, J. E. In National Institute of Standards and Technology, Gaithersburg MD, 20899 (http://webbook.nist.gov) 2000; NIST Standard Reference Database Number 69.

(46) Gioumousis, G.; Stevenson, D. P. *J. Chem. Phys.* **1958**, *29*, 294–299.

(47) Rothe, E. W.; Bernstein, R. B. *J. Chem. Phys.* **1959**, *31*, 1619–1627.

(48) Peng, C. Y.; Schlegel, H. B. *Israel J. Chem.* **1994**, *33*, 449.

(49) Peng, C. Y.; Ayala, P. Y.; Schlegel, H. B.; Frisch, M. J. *J. Comput. Chem.* **1996**, *17*, 49.

(50) Aristov, N.; Armentrout, P. B. *J. Phys. Chem.* **1987**, *91*, 6178.

(51) Georgiadis, R.; Armentrout, P. B. *J. Phys. Chem.* **1988**, *92*, 7060–7067.

(52) Haynes, C. L.; Armentrout, P. B.; Perry, J. K.; Goddard, W. A., III. *J. Phys. Chem.* **1995**, *99*, 6340–6346.

(53) Haynes, C. L.; Chen, Y.-M.; Armentrout, P. B. *J. Phys. Chem.* **1996**, *100*, 111–119.

(54) Chen, Y.-M.; Sievers, M. R.; Armentrout, P. B. *Int. J. Mass Spectrom. Ion Processes* **1997**, *167/168*, 195–212.

(55) Sunderlin, L. S.; Armentrout, P. B. *J. Phys. Chem.* **1988**, *92*, 1209–1219.

(56) Georgiadis, R.; Armentrout, P. B. *J. Phys. Chem.* **1988**, *92*, 7067–7074.

(57) Li, F.-X.; Zhang, X.-G.; Armentrout, P. B. *Int. J. Mass Spectrom.* **2006**, *255/256*, 279–300.

(58) Miller, T. M.; Bederson, B. *Adv. Atomic Molec. Phys.* **1977**, *13*, 1–55.

(59) Smith, D.; Adams, N. G.; Alge, E.; Villinger, H.; Lindinger, W. *J. Phys. (France)* **1980**, *B13*, 2787.

JP8052295